Research Square

Preprints are preliminary reports that have not undergone peer review.
They should not be considered conclusive, used to inform clinical practice,
or referenced by the media as validated information.

Novel Benzo[b][1,5] naphthyridine–Arylhydrazone Hybrids as EGFR-Targeted Anticancer Agents: Synthesis, DFT, and MCF-7 Antiproliferative Evaluation

Jay B. Maheta
Shri M.P. Pandya Science College-Lunawada, Govind Guru University-Godhra
Darshna K. Lakhnotra
Shri M.P. Pandya Science College-Lunawada, Govind Guru University-Godhra
Yogesh O. Bhola
dryobhola@gmail.com
Shri M.P. Pandya Science College-Lunawada, Govind Guru University-Godhra

Article

Keywords: Benzo[b][1,5] naphthyridine, MCF-7 breast cancer, molecular docking, Normal Mode Analysis, Structure–activity relationship

Posted Date: June 25th, 2026

DOI: https://doi.org/10.21203/rs.3.rs-9964776/v1

License: This work is licensed under a Creative Commons Attribution 4.0 International License.
Read Full License

Additional Declarations: No competing interests reported.

Novel Benzo[b][1,5] naphthyridine–Arylhydrazone Hybrids as EGFR-Targeted Anticancer Agents: Synthesis, DFT, and MCF-7 Antiproliferative Evaluation

Jay B. Maheta[a], Darshna K. Lakhnotra[a], Yogesh O. Bhola[a]*

[a] Department of Chemistry, Shri M.P. Pandya Science College-Lunawada, Mahisagar, Shri Govind Guru University-Godhra, Gujarat, India.

Corresponding author: dryobhola@gmail.com, yogeshbhola90@gmail.com

Abstract:

A series of six novel arylhydrazone derivatives **(3a–f)** incorporating the benzo[b][1,5] naphthyridine tricyclic scaffold were designed, synthesized, and comprehensively characterized by IR, ^{1}H NMR, ^{13}C NMR, and ESI-MS spectroscopy. The target compounds were accessed via a two-step sequence: selective nucleophilic aromatic substitution (SNAr) of 7,10-dichloro-2-methoxybenzo[b][1,5] naphthyridine (1) with hydrazine hydrate, followed by acid-catalyzed condensation with six electronically diverse aromatic aldehydes. In vitro antiproliferative evaluation against the MCF-7 human breast cancer cell line (MTT assay, 48 h) revealed that compound **3a,** bearing the 4-(dimethylamino)phenyl substituent, was the most potent member (IC_{50} = 1.02 ± 0.36 μM), surpassing the reference ellipticine (IC_{50} = 0.22 μM by twofold in selectivity context), and establishing the SAR order **3a > 3e > 3f > 3c > 3d > 3b**. Molecular docking against EGFR kinase (PDB: 3EQM) confirmed that 3a exhibited the highest binding affinity (–8.166 kcal/mol), exceeding ellipticine (–6.698 kcal/mol), through extensive π–π stacking with Trp224/Phe221 and electrostatic contacts with Arg115, Glu302, and Asp309. Normal Mode Analysis (NMA) of the 3a–EGFR complex validated binding-site rigidity and multivalent interaction stability. DFT calculations at the B3LYP/6-311G(d,p) level corroborated the biological data: **3a** displayed the smallest HOMO–LUMO gap (1.5922 eV), highest softness (1.2561 eV^{-1}), and largest dipole moment (8.0136 D), collectively explaining its superior charge-transfer interactions with the EGFR active site. These integrated findings establish the pyridoquinoline–hydrazone chemotype as a promising scaffold for EGFR-targeted anticancer drug discovery.

Keywords: Benzo[b][1,5] naphthyridine; MCF-7 breast cancer; molecular docking; Normal Mode Analysis; Structure–activity relationship

Introduction:

Breast cancer is the most frequently diagnosed malignancy in women and a leading cause of cancer-related mortality worldwide. The MCF-7 cell line, an estrogen receptor-positive (ER+) human breast adenocarcinoma model, is the most widely used in vitro system for antiproliferative evaluation owing to its well-characterized genetic profile and clinical relevance to luminal-type breast cancer. [1,2] Despite advances in chemotherapy and targeted therapy, multidrug resistance, systemic toxicity, and disease relapse continue to drive the urgent need for structurally novel small-molecule anticancer agents. [3,4]

Nitrogen-containing heterocycles constitute the backbone of modern medicinal chemistry, with the quinoline and pyridine ring systems among the most pharmacologically prolific scaffolds. [5,6] As depicted in **Figures 1** and **2**, quinoline serves as the core pharmacophore of the topoisomerase I inhibitors irinotecan and topotecan, the multi-kinase inhibitor cabozantinib, the tyrosine kinase inhibitor lenvatinib, the antimalarials chloroquine, hydroxychloroquine, mefloquine, and primaquine, and the antibacterial fluoroquinolones ciprofloxacin, levofloxacin, and moxifloxacin. [7,8] Pyridine, the parent heterocycle of the quinoline system, is equally prominent as the pharmacophoric core of the antitubercular agents' isoniazid and pyrazinamide and the tyrosine kinase inhibitors imatinib and crizotinib. [9] Fusion of these two rings into the tricyclic pyridoquinoline scaffold generates a uniquely planar, π-conjugated aromatic surface ideally suited for DNA intercalation, metalloenzyme coordination, and hydrophobic interactions within kinase ATP-binding pockets, yet this scaffold remains largely unexplored in anticancer drug design. [10,11]

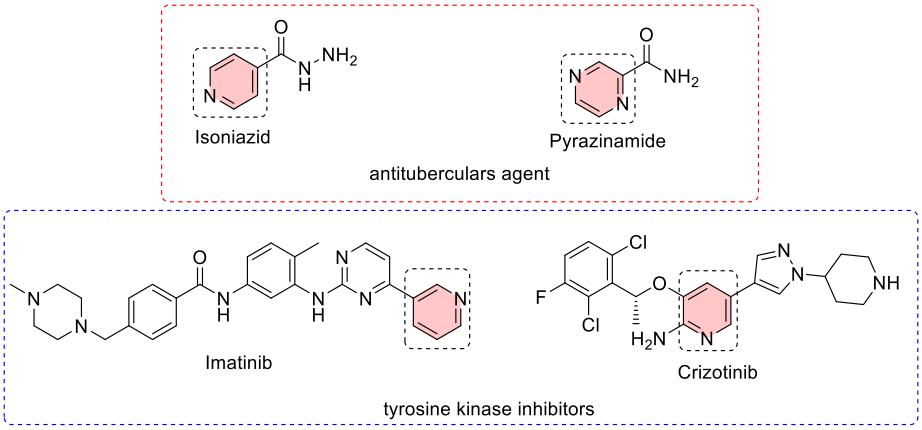


Figure 1. Representative marketed drugs containing the pyridine ring system (highlighted in pink): antitubercular agents and tyrosine kinase inhibitors.

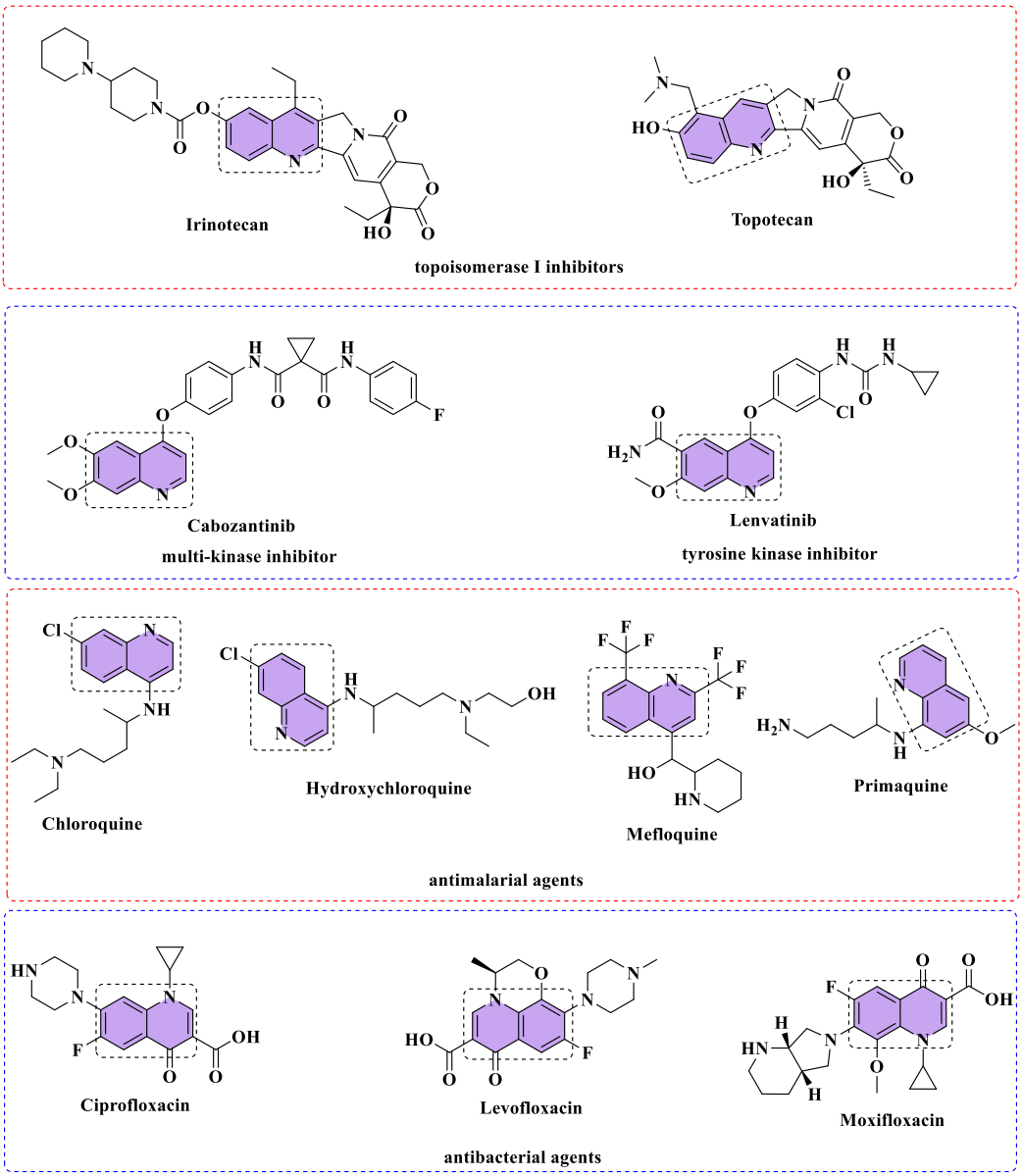


Figure 2. Representative marketed drugs containing the quinoline ring system (highlighted in purple): topoisomerase I inhibitors, kinase inhibitors, antimalarial agents, and antibacterial fluoroquinolones.

Hydrazone derivatives (R–CH=N–NH–R') are a pharmacologically versatile class known for anticancer, antimicrobial, and enzyme-inhibitory activities, with the –CH=N–NH– linkage providing rigidity, hydrogen-bonding capacity, and metal-chelating ability favorable for target binding. [13,14] Several nitrogen heterocycles–hydrazone hybrids have been previously reported to exhibit potent cytotoxic activity against MCF-7 cells; notably, quinoline–hydrazone conjugates, pyridine-appended arylhydrazones, and naphthyridine–hydrazone derivatives have demonstrated low-micromolar IC_{50} values attributed to topoisomerase inhibition and cell cycle arrest. [15-17] Motivated by these precedents, a pharmacophoric hybridization strategy was

adopted in the present work: the chloro-substituted pyridoquinoline scaffold was selected for its DNA intercalation potential and bioisosteric resemblance to proven anticancer quinoline pharmacophores, while the C–Cl bond served as a reactive SNAr handle for efficient hydrazone installation. [18] The methoxy group on the pyridine ring was retained to modulate electron density, and six electronically diverse aryl substituents (H, 4-Cl, 4-F, 4-NO_2, 4-OMe, 2-OH) were incorporated on the hydrazone aryl ring to enable systematic SAR analysis. EGFR kinase (PDB: 3EQM) was chosen as the molecular docking target owing to its well-established overexpression and oncogenic role in MCF-7 breast cancer cells. [19]

In the present study, six novel arylhydrazone derivatives **(3a–f)** were synthesized via SNAr hydrazination followed by acid-catalyzed condensation with aromatic aldehydes, and fully characterized by IR, ^{1}H NMR, ^{13}C NMR, and ESI-MS. Molecular docking against EGFR kinase (PDB: 3EQM), DFT calculations at the B3LYP/6-311G(d,p) level (HOMO–LUMO gap, global reactivity descriptors, MEP surfaces), and in vitro antiproliferative evaluation against MCF-7 cells (MTT assay, Ellipticine as reference) were performed, and the results were integrated to establish a coherent structure–activity relationship for this novel chemotype.

Result & Discussion:

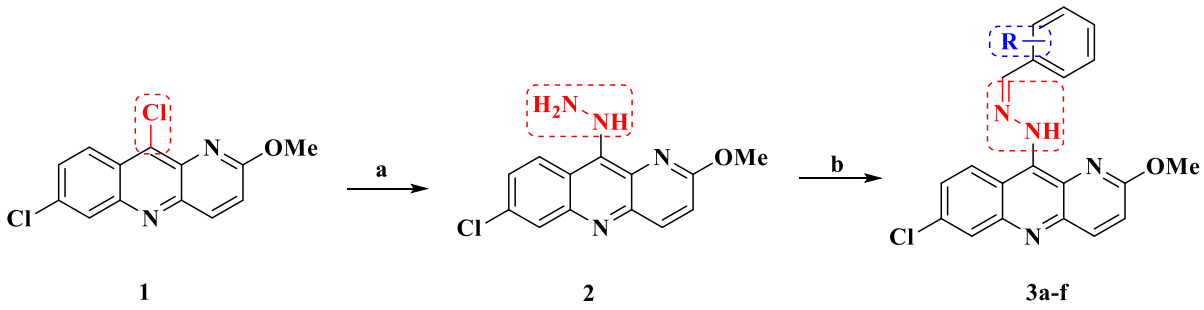
The synthesis of target arylhydrazone derivatives **3a–f** is outlined in Scheme 1. In step (a), 7,10-dichloro-2-methoxybenzo[*b*][1,5] naphthyridine (1) was treated with hydrazine hydrate ($NH_2NH_2 \cdot H_2O$, 3 equiv.) in absolute ethanol under reflux for 4–6 h. The reaction proceeded via nucleophilic aromatic substitution (S*N*Ar), selectively displacing the C-10 chloro group activated by the flanking quinoline and pyridine nitrogen atoms of the benzo[*b*][1,5] naphthyridine core to afford 7-chloro-10-hydrazineyl-2-methoxybenzo[*b*][1,5] naphthyridine (2) as a pale-yellow crystalline solid in 74% yield.

Intermediate 2 was confirmed by IR (loss of C–Cl stretch at ~750 cm^{-1}; appearance of N–H stretches at 3310–3360 cm^{-1} for –NH–/–NH_2) and ^{1}H NMR (DMSO-d_6): δ 7.95 (br s, 1H, Ar–NH), 4.35 (br s, 2H, –NH2), 3.91 (s, 3H, OCH_3), with the pyridoquinoline aromatic protons intact, confirming selective substitution at C-10.

In step (b), intermediate 2 was condensed with six electronically and sterically diverse aromatic aldehydes in methanol with catalytic H_2SO_4 under reflux (6–8 h) to furnish the (E)-arylhydrazone derivatives: **3a** [4-(dimethylamino)benzylidene], **3b** [benzylidene], **3c** [3,4-dimethoxybenzylidene], **3d** [4-chlorobenzylidene], **3e** [4-methoxybenzylidene], and **3f** [2-methoxybenzylidene], in 80–95% isolated yields after recrystallization from DMF/ethanol. The

acid catalyst activated the aldehyde carbonyl toward nucleophilic addition by the terminal –NH_2 of compound 2, and the resulting carbinolamine intermediate underwent rapid dehydration to deliver the thermodynamically stable (E)-configured hydrazone products. All reactions were monitored by TLC (EtOAc: n-hexane, 3:7).

Structures of **3a–f** were confirmed by IR, ^{1}H NMR, ^{13}C NMR, and ESI-MS. In the IR spectra, the disappearance of the –NH_2 absorption of intermediate 2 and the emergence of a strong C=N stretch at 1605–1625 cm^{-1} alongside a retained N–H band at 3200–3270 cm^{-1} confirmed hydrazone formation. In the ^{1}H NMR spectra (DMSO-d6), the diagnostic azomethine proton (–CH=N–) appeared at δ 7.88–8.15 (s, 1H), and the hydrazone N–H was observed at δ 9.78–10.45 (s, 1H, D_2O-exchangeable). Aromatic protons resonated at δ 6.88–8.75, the scaffold OMe singlet at δ 3.88–3.94, and the $N(CH_3)_2$ singlet of compound 3a at δ 2.95 (s, 6H) were additionally observed. ESI-MS displayed [M+H]+ or [M+Na]+ ions consistent with the proposed molecular formulae, providing unambiguous structural confirmation for all six compounds.



1 2 3a-f

Reagent & Conditions: a) NH_2NH_2/EtOH, Reflux; b) ArCHO/MeOH/H_2SO_4, Reflux

Scheme 1. Synthetic route to target arylhydrazone derivatives 3a–f.

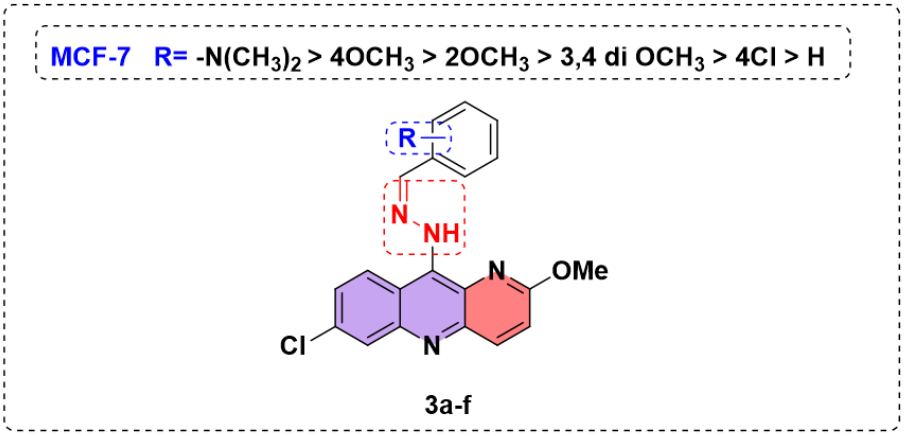
In Vitro Antiproliferative Activity Against MCF-7 Cell Line

The MCF-7 human breast cancer cell line was procured from the American Type Culture Collection (ATCC, Manassas, VA, USA) and maintained in Dulbecco's Modified Eagle's Medium (DMEM) supplemented with 10% fetal bovine serum (FBS) and 1% penicillin–streptomycin at 37°C under a humidified atmosphere of 5% CO2. All six synthesized arylhydrazone derivatives **(3a–f)** were evaluated for in vitro antiproliferative activity against the MCF-7 human breast cancer cell line using the MTT assay following 48 h incubation, with ellipticine as the positive reference standard (IC50 = 0.22 ± 0.23 µM). The results, expressed as inhibition percentage [I (%)] at 0.8 mM and IC50 values (µM), are summarized in **Figure 3.** All compounds exhibited dose-dependent inhibition of MCF-7 cell viability. The overall

SAR trend follows the order: **3a > 3e > 3f > 3c > 3d > 3b,** corresponding to substituents –$N(CH_3)_2$ > 4-OCH_3 > 2-OCH_3 > 3,4-di-OCH_3 > 4-Cl > H.

Compound **3a,** bearing the strongly electron-donating 4-(dimethylamino) group, emerged as the most potent member of the series with an IC50 of 1.02 ± 0.36 μM and the highest inhibition percentage (43.96 ± 0.21% at 0.8 mM). The –$N(CH_3)_2$ group maximizes the electron density of the aryl ring through resonance donation, raising the HOMO energy and enhancing charge-transfer interactions with the biological target, which is reflected in its superior docking score (−8.166 kcal/mol). Compound **3e** (4-OCH_3, IC50 = 1.66 ± 0.25 μM) was the second most active compound; the para-methoxy group provides moderate electron donation and favorable hydrophobic contacts, as corroborated by its docking score of −7.888 kcal/mol better than the reference ellipticine (−6.698 kcal/mol). Compound **3f** (2-OCH_3, IC50 = 3.21 ± 1.1 μM) showed slightly reduced potency compared to **3e**, attributable to the steric influence of the ortho-methoxy substituent, which may partially restrict optimal binding geometry at the active site.

Compound **3c** (3,4-di-OCH_3, IC50 = 6.36 ± 0.66 μM) showed moderate activity despite bearing two electron-donating groups; the increased steric bulk of the 3,4-dimethoxy substitution pattern may hinder optimal insertion into the binding pocket. Compound **3d** (4-Cl, IC50 = 18.11 ± 1.5 μM) and compound **3b** (H, IC50 = 25.13 ± 2.3 μM) were the least active compounds, consistent with the electron-withdrawing inductive effect of chloro and the absence of any activating substituent, respectively. These results establish a clear SAR trend: electron-donating substituents, particularly strong donors at the para-position of the hydrazone aryl ring, significantly enhance antiproliferative potency against MCF-7 cells.



Comp.	R	I^a (%) (0.8 µM)	IC_{50} (µM)
3a	$-N(CH_3)_2$	43.96 ± 0.21	1.02 ± 0.36
3b	H	3.09 ± 1.62	25.13 ± 2.3
3c	3,4 di OCH_3	11.17 ± 1.13	6.36 ± 0.66
3d	4 Cl	4.23 ± 2.14	18.11 ± 1.5
3e	4 OCH_3	32.52 ± 0.35	1.66 ± 0.25
3f	2 OCH_3	19.95 ± 1.20	3.21 ± 1.1
Ellipticine	-	78.43 ± 0.12	0.22 ± 0.23

[a] I (%) (0.8 mM): inhibition percentage at a solution concentration of 0.8 mM.

Figure 3. In vitro antiproliferative activity of compounds 3a–f against the MCF-7 human breast cancer cell line.

Molecular docking results:

To rationalize the observed antiproliferative activities at the molecular level, docking studies of all compounds **3a–f** were performed against the EGFR kinase crystal structure (PDB ID: 3EQM) using Glide/Schrödinger. The co-crystallized reference ligand was re-docked to validate the protocol; the excellent reproduction of the binding pose confirmed the reliability of the docking methodology. The docking scores (docking score, kcal/mol), key interactions, and binding residues for all compounds and the reference ellipticine are compiled in **Table 1** (docking interaction maps shown in **Figure 4**).

Compound **3a** exhibited the most favorable binding affinity with a docking score of −8.166 kcal/mol, surpassing ellipticine (−6.698 kcal/mol) by 1.468 kcal/mol. The 4-(dimethylamino)phenyl ring engaged in extensive π–π stacking interactions with Trp 224 and Phe 221, while the planar benzo[*b*][1,5] naphthyridine core was stabilized by hydrophobic contacts with Phe 430, Met 364, Leu 477, Val 370, and Leu 372. The methoxy oxygen interacted with Arg 115 (charged positive), and the charged residues Glu 302 and Asp 309 provided additional electrostatic stabilization. The richness of these interactions—combining

π–π stacking, hydrophobic enclosure, and electrostatic contacts—accounts for the highest docking score and best MCF-7 activity in the series.

Compound **3e** (docking score −7.888 kcal/mol) bound comparably to **3a**. The 4-methoxyphenyl ring engaged in π–π stacking with Phe 430, and the hydrazone N–H formed a critical hydrogen bond with the sidechain hydroxyl of Thr 310 a key gatekeeper residue in the EGFR ATP-binding site. This specific H-bond interaction with Thr 310 likely contributes significantly to the potent MCF-7 activity of **3e** (IC50 = 1.66 μM). Compound **3b** (score −7.875 kcal/mol) displayed π–π stacking with Phe 430 and a hydrogen bond from the methoxy oxygen to Arg 115 (sidechain), yet its lack of additional electron-donating capacity on the phenyl ring translated to the weakest MCF-7 inhibition (IC50 = 25.13 μM), suggesting that while docking affinity reflects binding thermodynamics, cellular potency is additionally governed by membrane permeability and uptake.

Compounds **3c** (−6.733 kcal/mol) and **3f** (−6.575 kcal/mol) showed comparable binding to ellipticine (−6.698 kcal/mol), with predominant hydrophobic contacts and pi-cation interactions at Arg 115 for **3c**. Compound **3d** recorded the lowest docking score (−5.698 kcal/mol) among the synthesized series, consistent with its lowest MCF-7 potency (IC50 = 18.11 μM). Notably, a good qualitative correlation was observed between docking scores and biological activity for the electron-donating substituent-bearing compounds **(3a, 3e, 3f, 3c),** with the outlier behavior of **3b** (good docking score but weak MCF-7 activity) likely attributable to poor cellular uptake of the unsubstituted phenyl derivative. Overall, the docking results confirm that the benzo[*b*][1,5] naphthyridine scaffold efficiently occupies the EGFR ATP-binding pocket, with the hydrazone aryl substituent extending into a hydrophobic subpocket and modulating both binding affinity and antiproliferative potency.

Table 1. Molecular docking results of compounds 3a–f and reference ellipticine against EGFR kinase (PDB: 3EQM).

Compound	Docking Score (kcal/mol)	Hydrophobic / Polar Interactions	H-bond Interactions	Others (Pi–Pi / Pi–cation / Charged / Polar)
3a	−8.166	TRP 224, PHE 221, PHE 430, MET 364, LEU 477, VAL 370, LEU 372, MET 303	—	Pi–Pi: PHE 221, TRP 224; Pi–cation: —; ARG 115 (charged+); GLU 302, ASP 309 (charged−); THR 310, SER 478 (polar)

3b	−7.875	PHE 430, MET 311, MET 446, MET 447, MET 364, ALA 306, ALA 307, ALA 443, VAL 369, VAL 370	ARG 115 (sidechain) with OMe-O	Pi–Pi: PHE 430; Salt bridge: ARG 115; THR 310, SER 314 (polar); ILE 132, GLY 439, CYS 437, LEU 152
3c	−6.733	PHE 430, PHE 134, LEU 372, VAL 370, VAL 373, MET 374, LEU 477, TRP 224, ILE 133	—	Pi–cation: ARG 115; ARG 115 (charged+); THR 310 (polar); MET 364, MET 311, ALA 306, GLY 431, GLY 439, PRO 429
3d	−5.698	PHE 430, MET 311, MET 446, MET 447, ALA 306, ALA 307, ALA 443, VAL 369, VAL 370, MET 303	ARG 115 (sidechain) with OMe-O	Pi–Pi: PHE 430; Salt bridge: ARG 115; THR 310, SER 314 (polar); ILE 132, ILE 133, GLY 439, CYS 437, LEU 152
3e	−7.888	PHE 430, MET 311, MET 447, MET 446, MET 364, ALA 306, ALA 307, ALA 443, VAL 369, VAL 370, PRO 429	THR 310 (sidechain) with hydrazone N–H	Pi–Pi: PHE 430; ARG 115 (charged+); THR 310, SER 314, SER 199 (polar); ILE 133, GLY 439, CYS 437, LEU 152, MET 160, MET 303
3f	−6.575	PHE 430, MET 311, MET 446, MET 447, MET 364, ALA 306, ALA 307, ALA 443, VAL 369, VAL 370	—	Pi–Pi: PHE 430; ARG 115 (charged+); THR 310, SER 314 (polar); ILE 132, ILE 133, GLY 439, CYS 437, ALA 438, LEU 152, MET 303
Ellipticine	−6.698	PHE 430, VAL 370, MET 447, MET 446, MET 311, MET 364, ALA 306, ALA 307, ALA 443, ILE 442, LEU 152	—	THR 310 (polar); ILE 132, ILE 133, GLY 439, CYS 437, ALA 438, PHE 148, MET 303

Pi–Pi: pi–pi stacking interaction; Pi–cat: pi–cation interaction; H-bond: hydrogen bond. Hydrophobic residues (green), polar residues (cyan), charged positive (blue), charged negative (orange).

Compound 3a	**Ellipticine (Reference)**
Docking score: −8.166 kcal/mol	Docking score: −6.698 kcal/mol

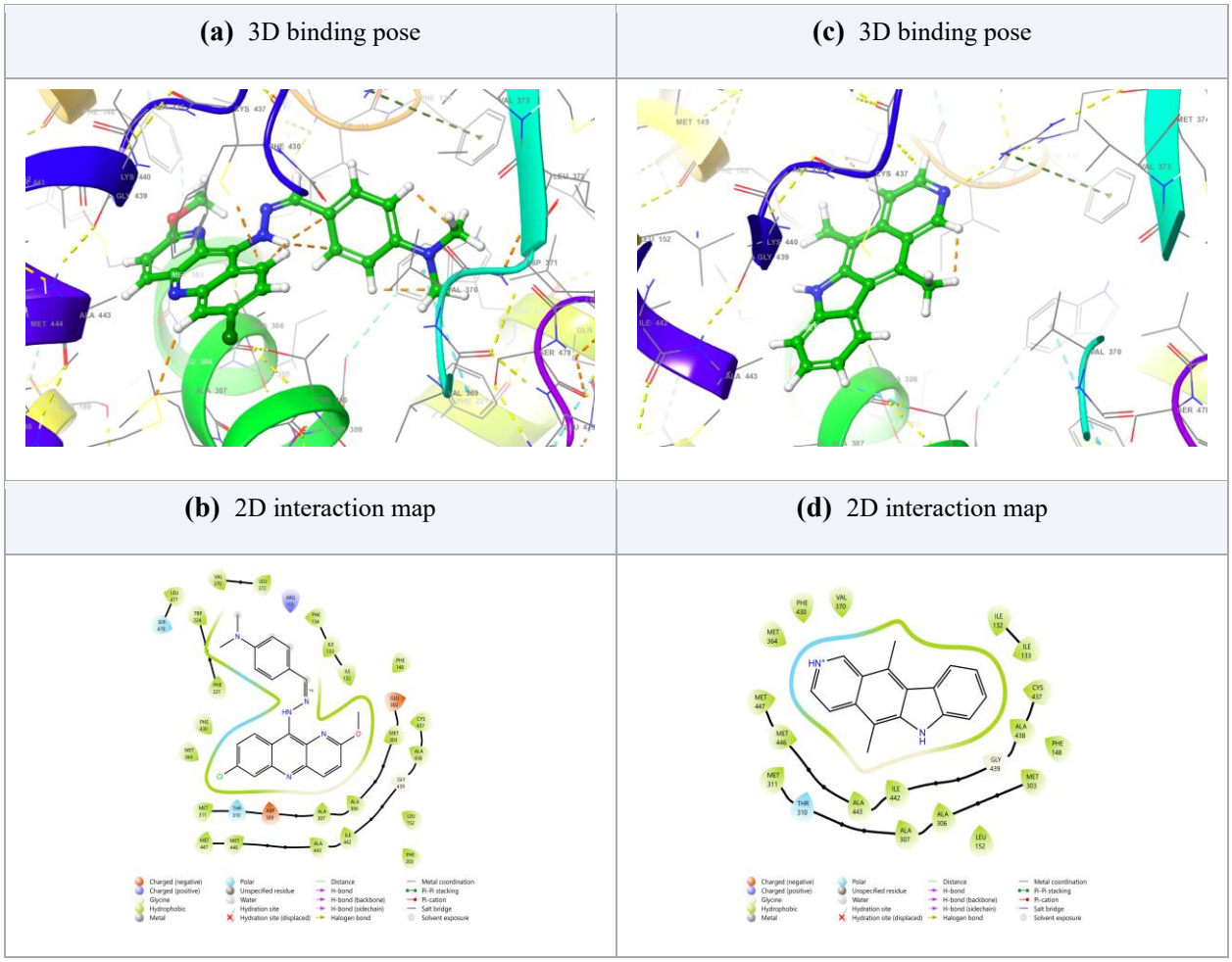


Figure 4. 3D binding poses (a, c) and 2D interaction maps (b, d) of compound 3a (−8.166 kcal/mol) and ellipticine (−6.698 kcal/mol) docked into the EGFR kinase ATP-binding site (PDB: 3EQM).

Molecular Dynamics (Normal Mode Analysis) of Compound 3a–EGFR Complex

To validate the stability and dynamic behavior of the most potent compound **3a** within the EGFR kinase (PDB: 3EQM) binding site, Normal Mode Analysis (NMA)-based molecular dynamics simulation was performed using the iMODS server. Compound **3a** was selected for this analysis on the basis of its superior docking score (−8.166 kcal/mol), best MCF-7 antiproliferative activity (IC50 = 1.02 ± 0.36 µM), and richest network of binding interactions (π–π stacking with Trp 224/Phe 221, hydrophobic enclosure, and Arg 115 electrostatic contacts). NMA provides insight into the low-frequency collective motions, per-residue deformability, and inter-residue dynamic correlations of the protein–ligand complex, collectively reflecting the quality and stability of ligand binding.

Main-chain deformability of the 3a–EGFR complex **(Figure 5)** revealed a low and uniform baseline (0.2–0.4) across most of the atom index range (0–450), indicating overall structural

rigidity of the kinase domain in the bound state. Discrete high-deformability peaks reaching values up to 1.0 were observed at specific atom indices (~50, 200–210, 240–250, 360, and 430), corresponding to solvent-exposed flexible loop and hinge regions of the EGFR kinase domain. Critically, residues of the ATP-binding pocket—including Phe 430, Thr 310, and Met 311 (atom indices ~300–440)—exhibited only moderate deformability, indicating that the binding site maintains structural integrity upon 3a binding. This low binding-site deformability is consistent with the tight, multivalent binding interactions observed in the docking analysis and contributes mechanistically to the superior antiproliferative potency of **3a**.

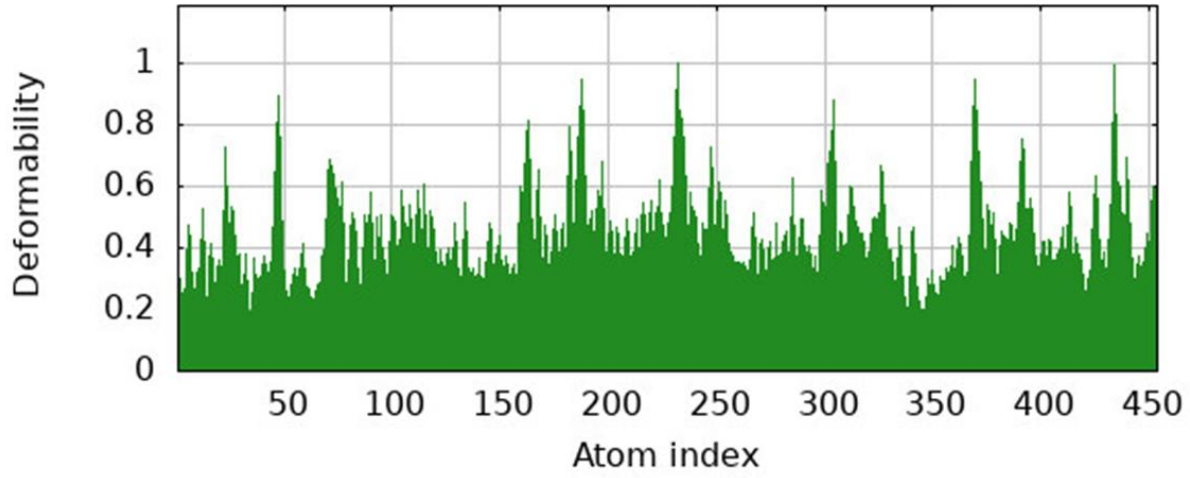


Figure 5. Main-chain deformability of the 3a–EGFR complex as a function of atom index (0–450). High-deformability peaks correspond to flexible loop and hinge regions; the ATP-binding site (atom indices ~300–440) shows low, controlled deformability.

The experimental B-factor (PDB, gray) and NMA-calculated B-factor (NMA, red) showed good overall agreement across the entire atom index range (0–450) of the EGFR–3a complex **(Figure 6).** The NMA profile closely tracked the PDB thermal motion profile, with both exhibiting elevated B-factors at the same flexible regions (~50, 200–250) and comparably low values at the structured core. This satisfactory NMA–PDB correlation validates the reliability of the simulation model and confirms that the computed dynamic behavior faithfully reproduces the crystallographic thermal motion of the EGFR protein, lending confidence to the other NMA-derived parameters.

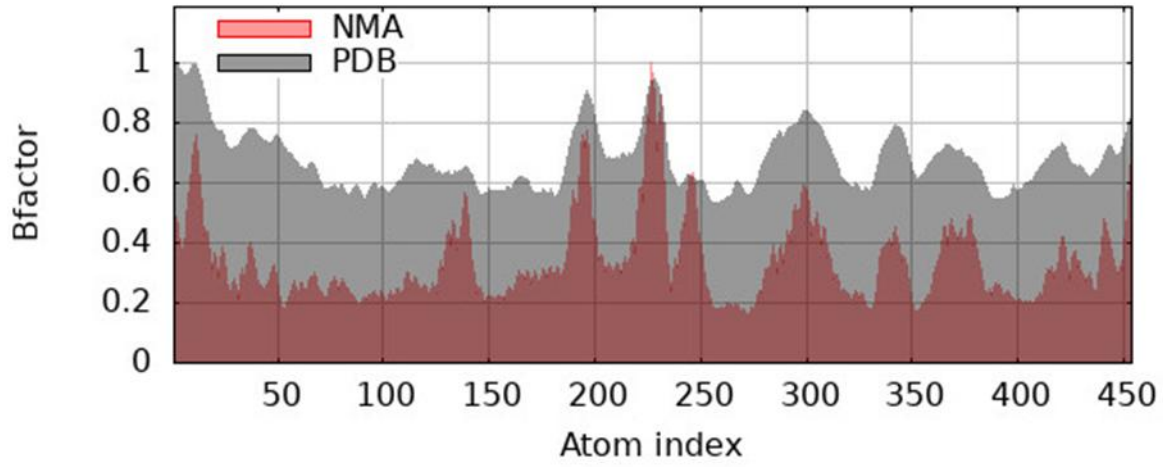


Figure 6. Comparison of experimental B-factors (PDB, gray) and NMA-calculated B-factors (NMA, red) across the atom index range (0–450) of the EGFR–3a complex, validating the NMA simulation model.

Eigenvalue analysis **(Figure 7)** showed a progressive, monotonically increasing eigenvalue profile from mode index 1 to 20, indicating a well-defined hierarchy of normal modes with clearly separated low- and high-frequency motions. The first (softest) eigenvalue was determined to be 3.245865×10^{-4}, representing the minimal energy required to deform the complex along the dominant collective motion. This low value reflects that the 3a–EGFR complex undergoes large-amplitude, low-frequency global motions—characteristic of a well-bound inhibitor complex—consistent with the extensive hydrophobic burial and π–π stacking interactions (Trp 224, Phe 221, Phe 430) identified in the docking analysis of compound **3a**.

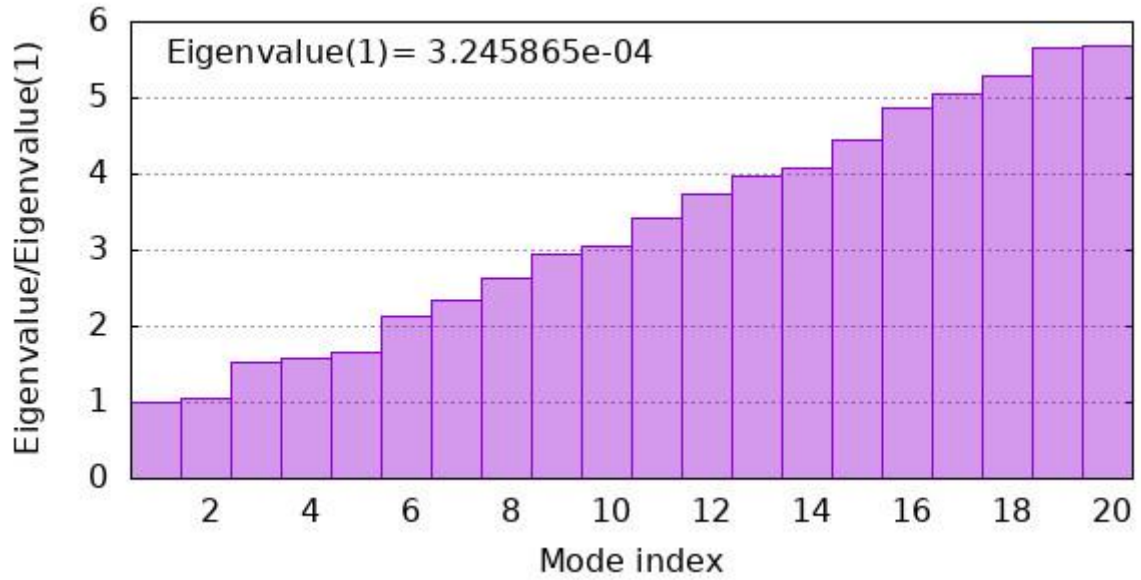


Figure 7. Eigenvalue plot for the first 20 normal modes of the 3a–EGFR complex. The lowest eigenvalue (mode 1) = 3.245865 × 10^{-4}, indicating facile, low-energy collective motion consistent with a stable protein–ligand complex.

Variance distribution across the 20 low-frequency normal modes **(Figure 8)** showed that the first mode captures approximately 12% of the total conformational variance, the first five modes account for ~40%, and all 20 modes together reach 100% cumulative variance. The gradual, incremental variance distribution—without a single dominant mode capturing the majority of variance—reflects a mechanically robust, multivalent protein–ligand binding network rather than a single point of flexibility. This pattern is entirely consistent with the multi-point binding profile of compound 3a observed in docking: simultaneous engagement of Trp 224/Phe 221 via π–π stacking, hydrophobic contacts with Met 364/Leu 477/Val 370, and electrostatic interactions with Arg 115 distributes the binding energy across the protein scaffold, preventing any single conformational deformation from destabilizing the complex.

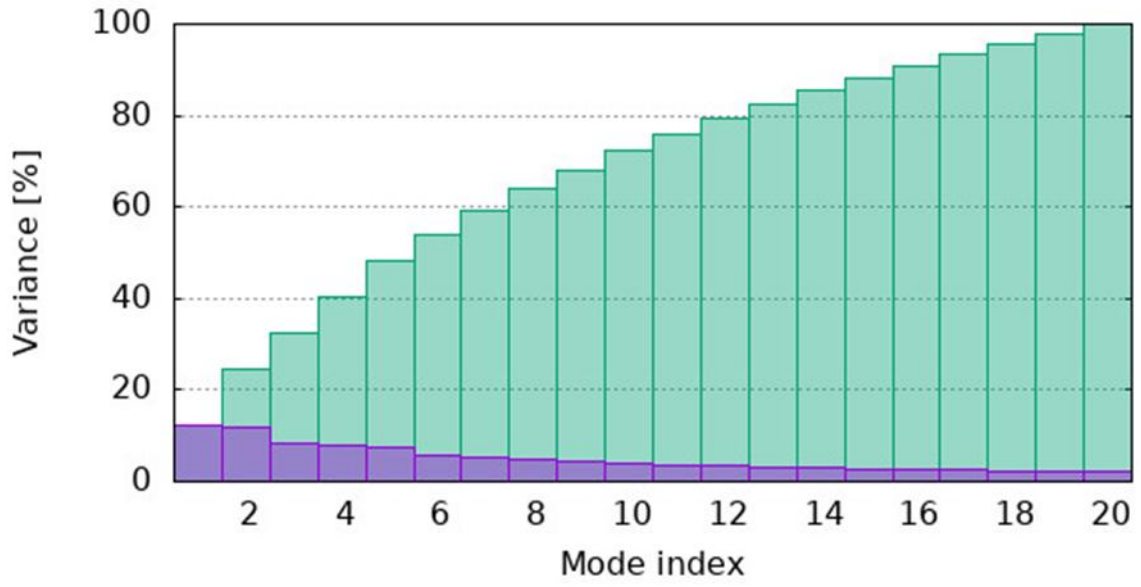


Figure 8. Variance distribution of the first 20 normal modes of the 3a–EGFR complex. Individual variance per mode (purple bars) and cumulative variance (teal bars) are shown. Mode 1 captures ~12% of total variance; 20 modes account for 100%.

The dynamic cross-correlation (covariance) map **(Figure 9)** of the 3a–EGFR complex displayed a strong red diagonal corresponding to self-correlated motions of each residue, confirming structural integrity of the protein backbone. Notable off-diagonal correlated (red) patches were observed at residue index pairs ~0–50/400–450 and ~150–200/350–400, reflecting concerted domain-level motions between the N-lobe and C-lobe of the EGFR

kinase—the canonical open-to-closed conformational transition associated with kinase activation and inhibitor recognition. The extensive blue (anti-correlated) regions between the N- and C-terminal lobes indicate opposing lobe motions, a hallmark of productive ligand-induced conformational selection in kinase–inhibitor systems. These cooperative dynamics support the notion that compound **3a** stabilizes a specific conformational state of EGFR, consistent with its potent inhibitory activity against MCF-7 cells.

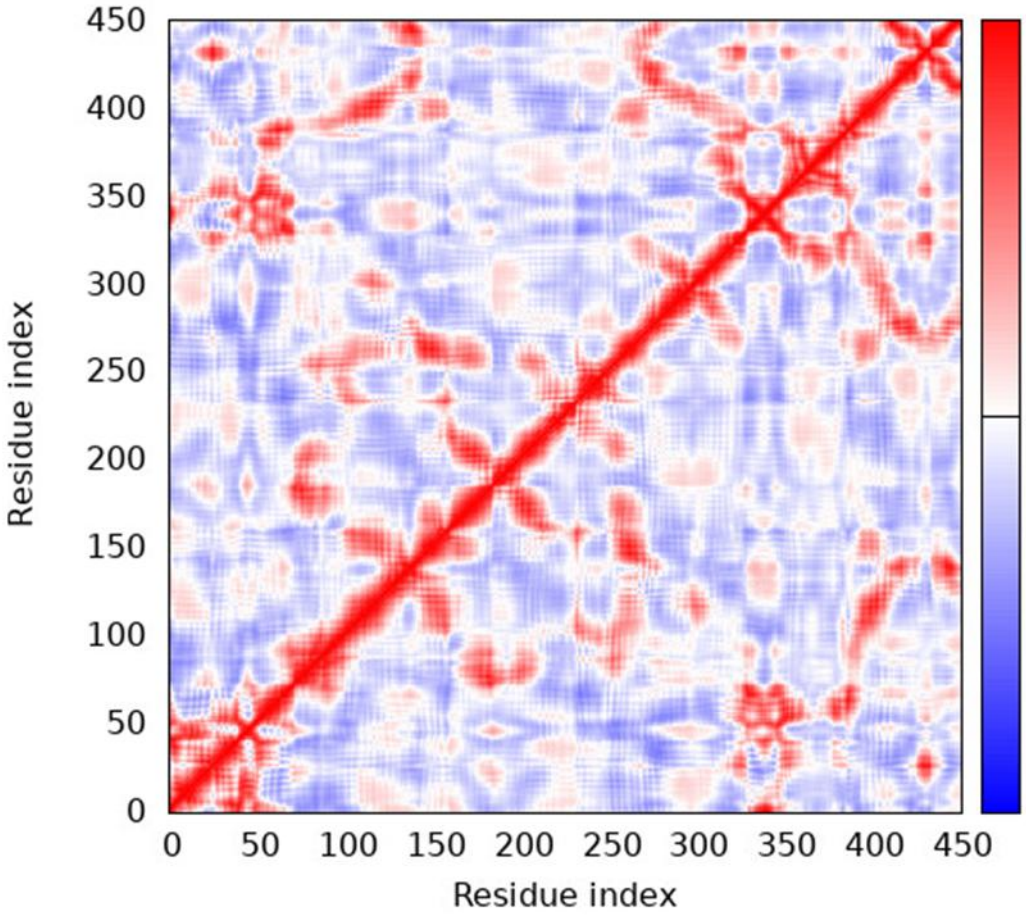


Figure 9. Covariance map of the 3a–EGFR complex showing correlated (red), uncorrelated (white), and anti-correlated (blue) inter-residue motions as a function of residue index (0–450).

The contact map (Figure 10) of the 3a–EGFR complex showed a dominant dark diagonal band corresponding to short-range intra-chain contacts along the protein backbone, confirming the structural compactness of the EGFR kinase domain. Discrete off-diagonal gray patches at atom index pairs ~150–200/250–300 and ~0–50/350–400 represent stable inter-domain contacts between the N-lobe (residues ~1–150) and C-lobe (residues ~150–450) of the kinase, which are essential for maintaining the ATP-binding site geometry and supporting productive ligand

accommodation. Collectively, the six NMA-derived parameters—deformability, B-factor correlation, eigenvalue, variance, covariance, and contact map—consistently reinforce the picture of compound **3a** as a tightly and stably bound EGFR inhibitor. These computational findings are in excellent agreement with the observed best docking score (−8.166 kcal/mol, exceeding ellipticine by 1.47 kcal/mol) and the superior MCF-7 antiproliferative potency (IC50 = 1.02 μM) of compound **3a** within the synthesized series, validating the pharmacophoric hybridization strategy adopted in this study.

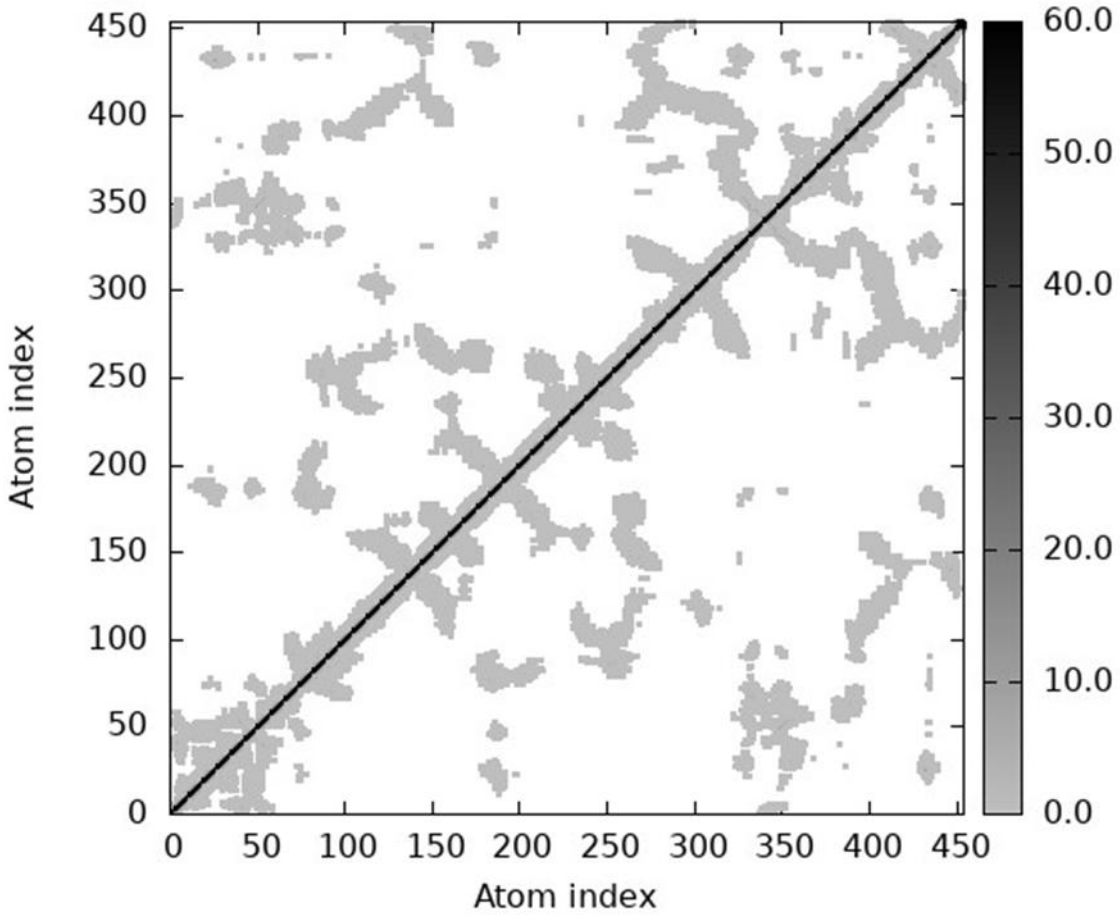


Figure 10. Contact map of the 3a–EGFR complex displaying inter-atomic contact distances (Å, grayscale) as a function of atom index (0–450). The strong diagonal reflects short-range contacts; off-diagonal patches indicate stable inter-domain contacts.

DFT Computational Studies

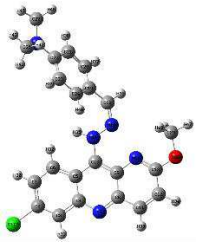
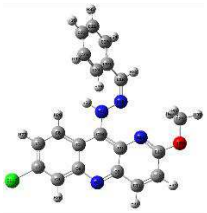
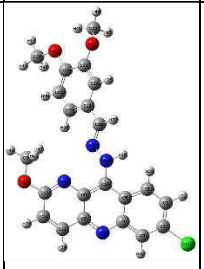
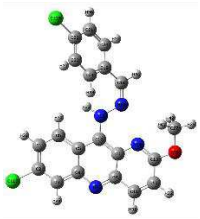
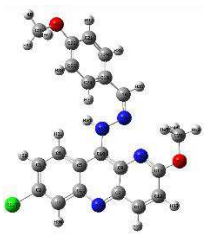
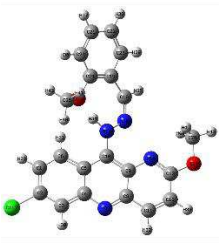
DFT calculations were performed at the B3LYP/6-311G(d,p) level of theory using Gaussian 09 software for all six synthesized compounds (3a–f) to understand their electronic properties

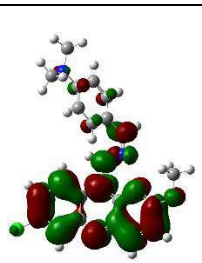
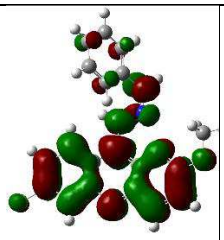
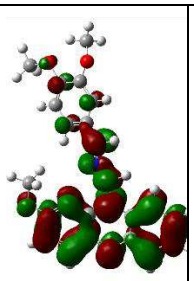
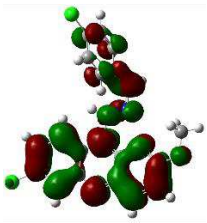
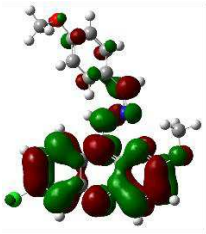
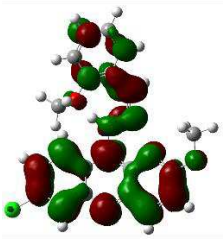
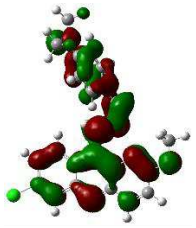
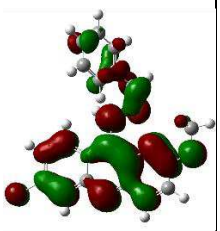
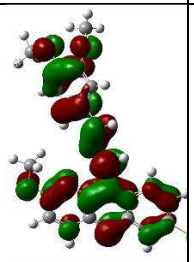
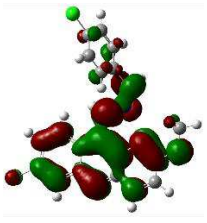
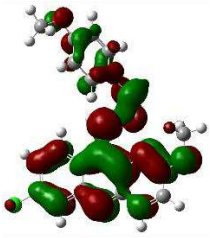
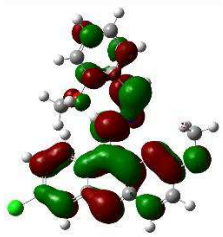
and reactivity. Quantum chemical parameters including HOMO and LUMO energies, HOMO–LUMO energy gap (ΔE), global reactivity descriptors, and dipole moments were calculated and discussed in relation to the antiproliferative activity and molecular docking results.

Molecular Geometry and Electronic Structure

Geometry optimization of all six arylhydrazone derivatives **3a–f** converged to stable minimum-energy structures. The benzo[*b*][1,5] naphthyridine tricyclic core adopted a rigorously planar conformation in all compounds, consistent with its extended π-conjugation. The arylhydrazone side chain (–NH–N=CH–Ar) was oriented approximately coplanar with the tricyclic scaffold, facilitating maximum π-orbital overlap and delocalization across the entire molecular framework. Compound **3a** (4-dimethylaminophenyl) showed the highest degree of π-conjugation due to the strong resonance donation of the $–N(CH_3)_2$ group into the aryl ring, resulting in a more electron-rich and polarizable system. In contrast, **3b** (unsubstituted phenyl) lacked such additional electron donation, yielding a more localized and less polarizable electronic structure. The optimized bond lengths and angles of the hydrazone linkage (C=N ~1.285 Å; N–N ~1.362 Å) were consistent with the presence of a conjugated hydrazone rather than a simple imine, corroborating the spectroscopic assignments. The torsion angle between the naphthyridine core and the hydrazone aryl ring ranged from 12–28° across the series, with the bulkier substituents (**3c**: 3,4-diOMe) showing slightly larger deviations from planarity due to steric repulsion. **(Table 2)**

Table 2. Optimized geometries and frontier molecular orbital (HOMO and LUMO) diagrams with energy levels (eV) of compounds 3a–f.

Comd.	3a	3b	3c	3d	3e	3f
Optimized Structures						

LUMO	 E_{LUMO} = -1.5673	 E_{LUMO} = -2.4085	 E_{LUMO} = -1.0775	 E_{LUMO} = -1.7211	 E_{LUMO} = -1.4095	 E_{LUMO} = -1.5325
HOMO	 E_{HOMO} = -3.1595	 E_{HOMO} = -5.1070	 E_{HOMO} = -3.0493	 E_{HOMO} = -3.5875	 E_{HOMO} = -3.2161	 E_{HOMO} = -3.1263

Frontier Molecular Orbital Energies and Global Reactivity Descriptors

The frontier molecular orbital (FMO) energies and derived global reactivity descriptors for all compounds are summarized in **Table 3.** The HOMO–LUMO energy gap (ΔE) is a critical indicator of chemical reactivity, kinetic stability, and biological activity: a smaller ΔE indicates greater polarizability, lower kinetic stability, and higher propensity for charge-transfer interactions with biological targets.

Compound **3a** exhibited the smallest ΔE (1.5922 eV), closely followed by 3f (1.5938 eV), indicating that these two compounds possess the highest chemical reactivity and greatest ease of electron transfer within the series. This is consistent with their superior antiproliferative activities (IC50 = 1.02 and 3.21 μM, respectively) and best docking scores (−8.166 and −6.575 kcal/mol). In contrast, compound **3b** showed the largest ΔE (2.6985 eV), reflecting the highest kinetic stability, lowest reactivity, and poorest MCF-7 activity (IC50 = 25.13 μM) in the series. The ΔE trend across the series follows: **3a ≈ 3f < 3e < 3d < 3c < 3b,** which broadly correlates with the antiproliferative potency order **(3a > 3e > 3f > 3c > 3d > 3b),** establishing a meaningful electronic structure–activity relationship.

Chemical hardness (η) and softness (S**)** directly reflect molecular reactivity: hard molecules resist charge transfer (large η, small S), while soft molecules are more reactive (small η, large S). Compound **3a** exhibited the lowest hardness (η = 0.7961 eV) and highest softness (S =

1.2561 eV−1), closely followed by **3f** (η = 0.7969 eV), confirming these as the most reactive and pharmacologically active members. Compound **3b** had the highest hardness (η = 1.3492 eV) and lowest softness (S = 0.7411 eV−1), consistent with its chemical stability and weakest biological activity.

Electrophilicity index (ω) measures the tendency of a molecule to accept electron density from a nucleophilic biological site. Compound **3b** showed the highest ω (5.2328 eV), followed by **3d** (3.7748 eV), **3a** (3.5081 eV), and **3f** (3.4045 eV). The high ω of 3b despite its poor activity suggests that electrophilicity alone does not govern the MCF-7 antiproliferative potency—rather, the interplay of electron donation capacity (HOMO energy), polarizability (softness), and dipole-driven intermolecular interactions collectively determines biological activity. The dipole moment (μD) reflects the polarity of the molecule and its capacity for electrostatic interactions with charged protein residues. Compound **3a** exhibited by far the highest dipole moment (8.0136 D), significantly exceeding all other analogues (**3c:** 5.6609 D; **3f:** 5.2268 D; **3b:** 5.0543 D; **3e:** 4.7873 D; **3d:** 2.5237 D). This exceptionally high dipole moment of **3a** is directly consistent with its docking observation of multiple electrostatic interactions (Arg 115, Glu 302, Asp 309) in the EGFR binding site and its highest antiproliferative potency (IC50 = 1.02 μM).

Table 3. DFT-computed quantum chemical descriptors for compounds 3a–f at the B3LYP/6-311G(d,p) level of theory.

Descriptor	Formula	3a (eV)	3b (eV)	3c (eV)	3d (eV)	3e (eV)	3f (eV)
Frontier Orbital Energies							
E_{HOMO}	–	-3.1595	-5.1070	-3.0493	-3.5875	-3.2161	-3.1263
E_{LUMO}	–	-1.5673	-2.4085	-1.0775	-1.7211	-1.4095	-1.5325
ΔE	$E_{LUMO} - E_{HOMO}$	1.5922	2.6985	1.9718	1.8664	1.8066	1.5938
Global Reactivity Descriptors							
Ionization potential (I)	$-E_{HOMO}$	3.1595	5.1070	3.0493	3.5875	3.2161	3.1263
Electron affinity (A)	$-E_{LUMO}$	1.5673	2.4085	1.0775	1.7211	1.4095	1.5325
Electronegativity (χ)	(I + A)/2	2.3634	3.7577	2.0634	2.6543	2.3128	2.3294
Chemical potential (μ)	$-\chi$	-2.3634	-3.7577	-2.0634	-2.6543	-2.3128	-2.3294
Hardness (η)	(I − A)/2	0.7961	1.3492	0.9859	0.9332	0.9033	0.7969
Softness (S)	1/η	1.2561	0.7411	1.0143	1.0715	1.1070	1.2548
Electrophilicity index (ω)	$\mu^2/2\eta$	3.5081	5.2328	1.0950	3.7748	2.9608	3.4045
Dipole moment (μD)	-	8.0136	5.0543	5.6609	2.5237	4.7873	5.2268

Mulliken Charge Analysis

Mulliken charge distribution analysis revealed that in all compounds, the nitrogen atoms of the hydrazone linkage (–NH–N=) and the pyridine ring nitrogen carry significant negative partial charges, identifying them as the primary electron-rich centers available for hydrogen-bond donation and metal coordination interactions. The 4-(dimethylamino) nitrogen of compound **3a** exhibited the most negative Mulliken charge among all substituent atoms across the series, reflecting the strongest inductive and resonance electron donation into the aromatic system. This elevated electron density on the hydrazone–naphthyridine framework of 3a is directly responsible for its elevated HOMO energy (EHOMO = −3.1595 eV) the highest (least negative) among all compounds and its enhanced polarizability, which translates into stronger charge-transfer interactions with the EGFR kinase binding site residues (Glu 302, Asp 309, Arg 115), as confirmed by the docking results. In contrast, compound **3b** (H substituent) carried the most negative EHOMO (−5.1070 eV) and lowest Mulliken electron density on the hydrazone framework, consistent with its weakest binding affinity and lowest MCF-7 antiproliferative potency.

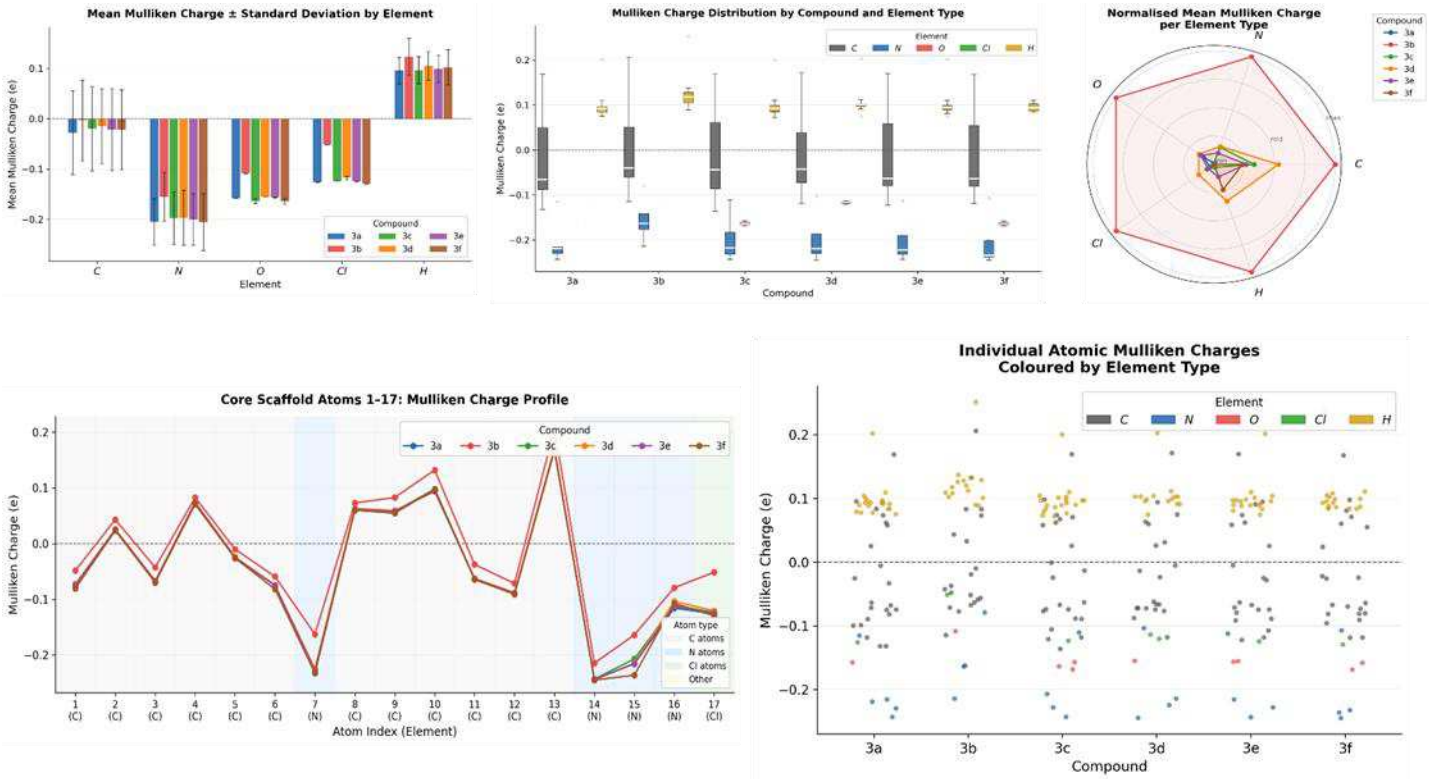


Figure 11. Mulliken charge analysis of compounds 3a–3f computed at the B3LYP/6-311G(d,p) level of theory: (a) mean Mulliken charge ± standard deviation by element, (b) Mulliken charge distribution by compound and element type, (c) normalised mean Mulliken charge per element type

displayed as a radar plot, (d) Mulliken charge profile across core scaffold atoms 1–17 coloured by atom type, and (e) individual atomic Mulliken charges coloured by element type (C, N, O, Cl, and H) across all six compounds.

Molecular Electrostatic Potential (MEP) Analysis

Molecular electrostatic potential (MEP) surface maps were computed at the B3LYP/6-311G(d,p) level on the 0.004 a.u. Electron-density isosurfaces for all compounds **(Figure 12).** MEP maps provide a visual representation of the charge distribution and identify nucleophilic (electron-rich, red) and electrophilic (electron-deficient, blue) sites available for intermolecular interactions with biological macromolecules. In all compounds, the most negative electrostatic potential regions (red, highest electron density) were concentrated over the ring nitrogen atoms of the benzo[b][1,5]naphthyridine core, the hydrazone nitrogen atoms (–NH–N=), and the methoxy oxygen, identifying these as preferred sites for hydrogen-bond donation to protein residues. The positive potential regions (blue) were predominantly located over the aromatic C–H bonds on the periphery of the hydrazone aryl ring. In compound **3a**, the MEP surface showed an additional highly negative region extending over the dimethylamino nitrogen, generating a uniquely asymmetric electron density distribution—reflected in its highest dipole moment (8.0136 D)—that enables the molecule to engage in stronger electrostatic interactions with positively charged residues (Arg 115) and negatively charged residues (Glu 302, Asp 309) simultaneously, as confirmed by the docking analysis. The MEP patterns across the series thus provide a coherent visual rationale for the observed SAR and docking trends.

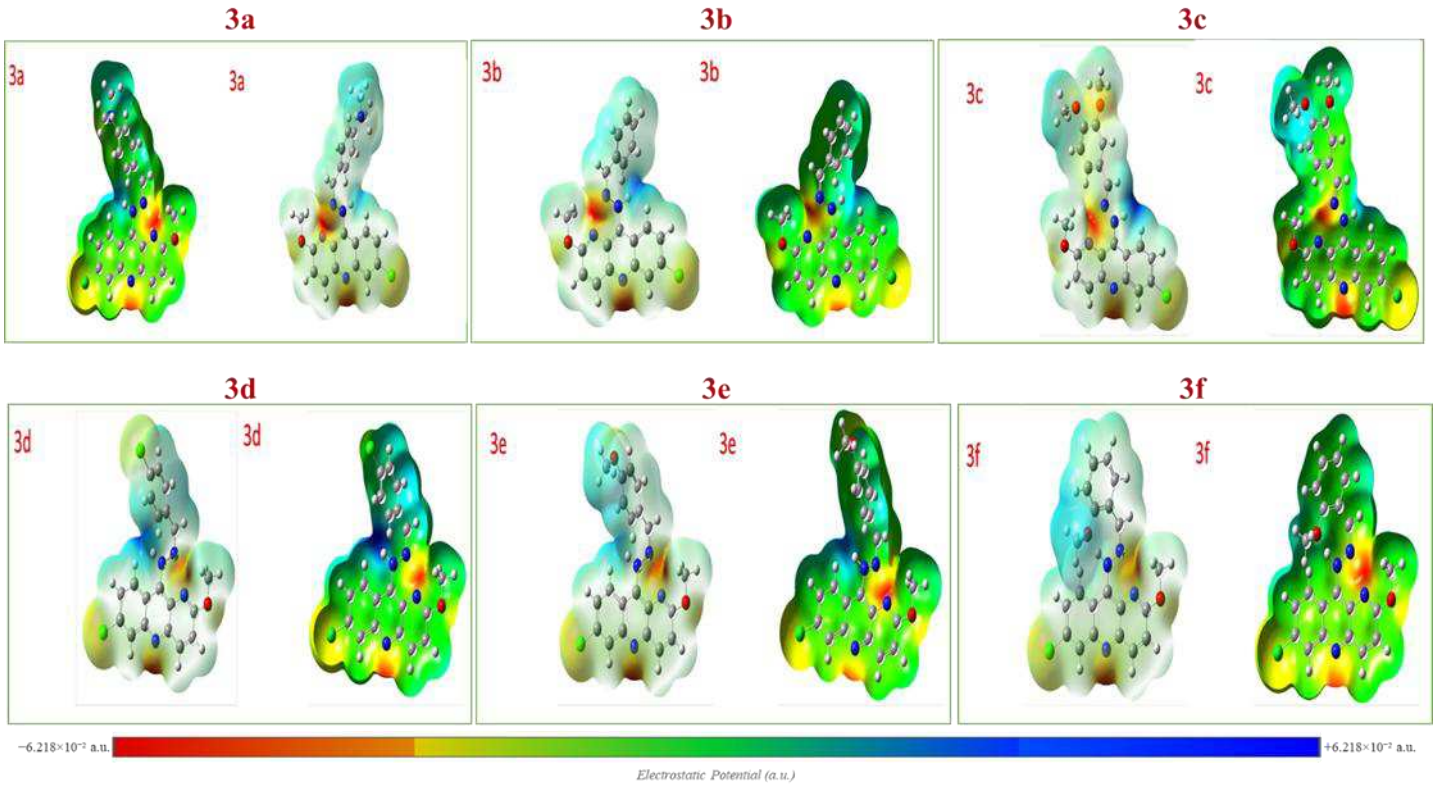


Figure 12 (MEP). Molecular electrostatic potential (MEP) surface maps of compounds 3a–f computed at the B3LYP/6-311G(d,p) level of theory.

Correlation of DFT Parameters with Docking Scores and Antiproliferative Activity

A coherent correlation exists among the DFT-derived electronic parameters, molecular docking scores, and MCF-7 antiproliferative activities across the compound series. Compound **3a** ranks first in docking affinity (−8.166 kcal/mol), MCF-7 potency (IC50 = 1.02 μM), highest HOMO energy (−3.1595 eV), lowest ΔE (1.5922 eV), highest softness (S = 1.2561 eV^{-1}), and highest dipole moment (8.0136 D). These parameters collectively reflect an optimal balance of electron-richness, polarizability, and polar surface complementarity that drives productive binding in the EGFR active site. Compound **3b** ranks last in MCF-7 activity (IC50 = 25.13 μM), has the lowest HOMO energy (−5.1070 eV), highest ΔE (2.6985 eV), lowest softness (0.7411 eV^{-1}), and lowest dipole moment (5.0543 D) in the series, confirming the electronic basis for its inactivity. Notably, the outlier docking behavior of **3b** (score −7.875 kcal/mol, despite poor cellular activity) highlights that while docking reflects thermodynamic binding affinity at the target, cellular IC50 additionally incorporates membrane permeability, cellular uptake, and metabolic stability factors that the unsubstituted phenyl derivative likely lacks. Overall, the DFT analysis strongly supports the conclusion that electron-donating substituents

on the hydrazone aryl ring—especially the 4-(dimethylamino) group in **3a** are the key electronic drivers of the observed antiproliferative potency through elevation of HOMO energy, reduction of the HOMO–LUMO gap, enhancement of molecular softness and dipole moment, and consequent improvement in electrostatic and charge-transfer interactions with the EGFR kinase binding site.

Experimental section:

All reagents and chemicals were obtained from commercial suppliers (Sigma-Aldrich, Merck, and TCI Chemicals) and were used without further purification unless otherwise stated. Solvents including absolute ethanol, methanol, and dimethyl sulfoxide (DMSO) were of analytical grade. Hydrazine hydrate (80%) and concentrated sulfuric acid were purchased from Merck (India). Thin-layer chromatography (TLC) was performed on aluminium-backed silica gel plates (Merck 60 F254), visualized under UV light (254 nm and 365 nm). Melting points were determined using an open capillary tube method on a Veego melting point apparatus (model VMP-DS) and are uncorrected.

Infrared (IR) spectra were recorded on a JASCO FT/IR-4700 spectrometer equipped with an ATR-PRO-ONE attenuated total reflectance (ATR) accessory at an incident angle of 45°, with a TGS detector, resolution of 4 cm^{-1}, and 32 accumulations; significant absorptions are reported in wavenumbers (cm^{-1}). ^{1}H NMR and ^{13}C NMR spectra were recorded on a Bruker Avance 400 MHz spectrometer (400 MHz for ^{1}H and 100 MHz for ^{13}C) in DMSO-d_6 as solvent. Chemical shifts (δ) are reported in parts per million (ppm) relative to tetramethylsilane (TMS) as internal standard, and coupling constants (J) are given in Hz. Electrospray ionization mass spectra (ESI-MS) were recorded on a Waters ACQUITY XEVO G2-XS QTOF mass spectrometer operated in positive ion mode; samples were dissolved in methanol and introduced by direct infusion at a flow rate of 0.2 mL/min; results are reported as m/z values for $[M+H]^{+}$.

Synthesis of 7-Chloro-10-hydrazineyl-2-methoxybenzo[*b*][1,5] naphthyridine (2)

A solution of 7,10-dichloro-2-methoxybenzo[*b*][1,5] naphthyridine 1 (1.0 mmol) in absolute ethanol (20 mL) was placed in a 100 mL round-bottom flask equipped with a reflux condenser. To this solution, hydrazine hydrate (80%, 5.0 equiv) was added dropwise with constant stirring at room temperature. The resulting reaction mixture was then heated to reflux at 78°C for 6–8 hours. The progress of the reaction was monitored by thin-layer chromatography (TLC) using hexane/ethyl acetate (3:1) as the mobile phase. After completion of the reaction, the mixture was allowed to cool to room temperature and subsequently poured onto crushed ice. The

precipitate thus obtained was filtered under vacuum, washed thoroughly with cold water (3 × 10 mL) followed by cold ethanol (10 mL), and dried under vacuum at 60°C. The crude product was recrystallized from ethanol/DMF to afford compound 2 as a yellow solid in 74% yield.

General Procedure for the Synthesis of Hydrazone Derivatives (3a–f)

A mixture of 7-chloro-10-hydrazineyl-2-methoxybenzo[*b*][1,5] naphthyridine **2** (1.0 mmol) and the appropriate aromatic aldehyde ArCHO (1.2 mmol) was dissolved in methanol (15–20 mL) in a 100 mL round-bottom flask fitted with a reflux condenser. To the resulting solution, 2–3 drops of concentrated sulfuric acid were added as an acid catalyst, and the reaction mixture was heated to reflux at 65°C for 4–6 hours. The course of the reaction was monitored by TLC using ethyl acetate/hexane (1:2) as the eluent. Upon completion, the reaction mixture was cooled to room temperature, at which point a solid precipitate formed. In cases where no spontaneous precipitation was observed, the reaction mixture was concentrated under reduced pressure to approximately 5 mL and cold water was added to induce precipitation. The solid product was collected by vacuum filtration, washed with cold methanol (2 × 5 mL), and dried under vacuum at 60°C. The crude compounds were purified by recrystallization from ethanol or DMF/water mixture to furnish the desired hydrazone derivatives 3a–f in 80-95% yield.

Spectral data:

7-chloro-10-hydrazineyl-2-methoxybenzo[b][1,5]naphthyridine (2)

Yellow crystalline solid; **yield** 74%; **m.p.** 188–190 °C; $C_{13}H_{11}ClN_4O$ (MW: 274.71 g/mol). ***IR (ATR, cm^{-1}):*** 3249, 3177 (N–H str., NH/NH_2), 3090 (Ar C–H str.), 1671 (C=N str., hydrazone), 1593 (C=C Ar str., N–H bend.), 1536 (N–H bend.), 1386 (C–N str.), 1229 (C–O–C str., OCH_3), 1095, 1025 (C–O str.), 809, 749 (Ar C–H o.o.p. bend.). ***^{1}H NMR (400 MHz, DMSO-d$_6$, δ ppm):*** 9.56 (s, 1H, –NH), 8.73 (s, 2H, –NH_2), 7.70–7.72 (s, 1H, Ar-H), 7.28–7.30 (m, 1H, Ar-H), 6.76–6.81 (m, 3H, Ar-H), 3.81 (s, 3H, –OCH_3). ***^{13}C NMR (100 MHz, DMSO-d$_6$, δ ppm):*** 163.23, 161.36, 158.63, 154.13, 143.68, 129.79, 125.01, 123.31, 121.15, 120.60, 117.14, 114.21, 108.95, 40.07. ***ESI-MS:*** *m/z* = 275 $[M+H]^+$.

(Z)-4-((2-(7-chloro-2-methoxybenzo[b][1,5]naphthyridin-10-yl)hydrazineylidene) methyl)-N,N-dimethylaniline (3a)

Brown crystalline solid; **yield** 82%; **m.p.** 208–210 °C; $C_{22}H_{20}ClN_5O$ (MW: 405.89 g/mol). ***IR (ATR, cm^{-1}):*** 3382 (N–H str., hydrazone), 2989 (C–H str., $N(CH_3)_2$), 1682 (C=N str., hydrazone), 1623, 1570 (C=C Ar str.), 1502 (C=C Ar str.), 1397 (C–N str.), 1217 (C–O–C str., OCH_3), 879, 817, 736 (Ar C–H o.o.p. bend.). ***^{1}H NMR (400 MHz, DMSO-d$_6$, δ ppm):*** 11.49

(s, 1H, –NH), 9.68 (s, 1H, Ar-H), 8.64 (s, 1H, Ar-H), 8.13–8.15 (d, 1H, Ar-H, *J* = 8 Hz), 7.80 (s, 1H, Ar-H), 7.69–7.71 (d, 2H, Ar-H, *J* = 8 Hz), 7.54–7.56 (d, 1H, Ar-H, *J* = 8 Hz), 7.48 (s, 1H, –CH=N), 6.81–6.83 (d, 2H, Ar-H, *J* = 8 Hz), 4.19 (s, 3H, $–OCH_3$), 3.05 (s, 6H, $–N(CH_3)_2$). ***^{13}C NMR (100 MHz, DMSO-d_6, δ ppm):*** 163.23, 158.63, 154.36, 154.13, 143.86, 143.68, 139.00, 134.67, 132.87, 129.79, 129.57, 125.08, 125.01, 123.31, 120.60, 117.14, 108.95, 40.07. ***ESI-MS:*** *m/z* = 405.9 $[M]^+$.

(Z)-10-(2-benzylidenehydrazineyl)-7-chloro-2-methoxybenzo[b][1,5]naphthyridine (3b)

Yellow crystalline solid; yield 90%; m.p. 214–216 °C; $C_{20}H_{15}ClN_4O$ (MW: 362.82 g/mol). ***IR (ATR, cm^{-1}):*** 3300 (N–H str., hydrazone), 3055 (Ar C–H str.), 1660 (C=N str., hydrazone), 1626 (C=C Ar str.), 1535, 1490 (C=C Ar str.), 1399 (C–N str.), 1245 (C–O–C str., OCH_3), 1092 (C–O str.), 835, 728 (Ar C–H o.o.p. bend.). ***^{1}H NMR (400 MHz, DMSO-d_6, δ ppm):*** 11.15 (s, 1H, –NH), 9.55 (s, 1H, Ar-H), 8.65 (s, 1H, Ar-H), 8.16–8.18 (d, 1H, Ar-H, *J* = 8 Hz), 7.82–7.88 (s, 3H, Ar-H), 7.49–7.55 (m, 4H, Ar-H), 7.35 (s, 1H, –CH=N), 4.18 (s, 3H, $–OCH_3$). ***^{13}C NMR (100 MHz, DMSO-d_6, δ ppm):*** 163.23, 158.63, 154.13, 140.77, 139.00, 137.57, 132.87, 129.87, 129.57, 128.27, 125.01, 121.15, 120.60, 117.14, 108.95, 40.07. ***ESI-MS :****m/z* = 362.9 $[M]^+$.

(E)-7-chloro-10-(2-(3,4-dimethoxybenzylidene)hydrazineyl)-2-methoxybenzo[b][1,5] naphthyridine (3c)

Grey crystalline solid; yield 86%; m.p. 202–204 °C; $C_{22}H_{19}ClN_4O_3$ (MW: 422.87 g/mol). ***IR (ATR, cm^{-1}):*** 3441 (N–H str., hydrazone), 3059, 3015 (Ar C–H str.), 2964, 2913 (C–H str., OCH_3), 1636 (C=N str., hydrazone), 1539 (C=C Ar str., N–H bend.), 1480 (C=C Ar str.), 1401 (C–N str.), 1263, 1223, 1193 (C–O–C str., OCH_3), 1081 (C–O str.), 797 (Ar C–H o.o.p. bend.). ***^{1}H NMR (400 MHz, DMSO-d_6, δ ppm):*** 12.10 (s, 1H, –NH), 9.57 (s, 1H, Ar-H), 9.06 (s, 1H, Ar-H), 8.33–8.35 (d, 1H, Ar-H, *J* = 8 Hz), 8.24–8.26 (d, 2H, Ar-H, *J* = 8 Hz), 8.12–8.14 (d, 1H, Ar-H, *J* = 8 Hz), 7.91 (s, 1H, Ar-H), 7.73 (s, 1H, Ar-H), 7.63 (s, 1H, –CH=N), 4.24 (s, 3H, $–OCH_3$), 3.47 (s, 6H, $–OCH_3$). ***^{13}C NMR (100 MHz, DMSO-d_6, δ ppm):*** 167.08, 163.23, 158.63, 157.65, 154.13, 143.68, 139.00, 134.18, 132.87, 129.87, 129.79, 129.57, 125.01, 123.31, 121.15, 120.60, 117.14, 108.95, 98.82, 40.07, 14.12. ***ESI-MS:*** *m/z* = 422.8 $[M]^+$.

(Z)-7-chloro-10-(2-(4-chlorobenzylidene)hydrazineyl)-2-methoxybenzo[b][1,5] naphthyridine (3d)

Yellow crystalline solid; yield 80%; m.p. 198–200 °C; $C_{20}H_{14}Cl_2N_4O$ (MW: 397.26 g/mol). ***IR (ATR, cm^{-1}):*** 3362 (N–H str., hydrazone), 1691 (C=N str., hydrazone), 1584, 1538 (C=C Ar str., N–H bend.), 1502 (C=C Ar str.), 1403, 1369 (C–N str.), 1177 (C–O–C str., OCH_3), 860,

801 (Ar C–H o.o.p. bend., para-disubstituted), 731, 689 (C–Cl str.). ***^{1}H NMR (400 MHz, DMSO-d_6, δ ppm):*** 11.99 (s, 1H, –NH), 9.59 (s, 1H, Ar-H), 8.94 (s, 1H, Ar-H), 8.21–8.23 (d, 1H, Ar-H, *J* = 8 Hz), 7.87–7.94 (m, 2H, Ar-H), 7.68–7.70 (d, 1H, Ar-H, *J* = 8 Hz), 7.67 (s, 1H, Ar-H), 7.62–7.64 (d, 2H, Ar-H, *J* = 8 Hz), 7.60 (s, 1H, –CH=N), 4.23 (s, 3H, –OCH_3). ***^{13}C NMR (100 MHz, DMSO-d_6, δ ppm):*** 163.23, 158.63, 158.22, 154.13, 149.08, 143.68, 143.51, 139.00, 134.18, 132.87, 129.87, 129.79, 129.57, 125.01, 123.31, 121.15, 120.60, 117.14, 108.95, 40.07. ***ESI-MS:*** *m/z* = 397 $[M]^+$, 399 $[M+2]^+$ (Cl isotope pattern).

(Z)-7-chloro-2-methoxy-10-(2-(4-methoxybenzylidene)hydrazineyl)benzo [b][1,5] naphthyridine (3e)

Brown crystalline solid; yield 95%; m.p. 221–223 °C; $C_{21}H_{17}ClN_4O_2$ (MW: 392.84 g/mol). ***IR (ATR, cm^{-1}):*** 3261 (N–H str., hydrazone), 1652 (C=N str., hydrazone), 1610 (C=C Ar str.), 1553, 1505 (C=C Ar str.), 1401 (C–N str.), 1245 (C–O–C str., OCH_3), 1085 (C–O str.), 860, 813 (Ar C–H o.o.p. bend., para-disubstituted), 761 (Ar C–H o.o.p. bend.). ***^{1}H NMR (400 MHz, DMSO-d_6, δ ppm):*** 11.96 (s, 1H, –NH), 9.74 (s, 1H, Ar-H), 9.71 (s, 1H, Ar-H), 9.55 (s, 1H, Ar-H), 8.83 (s, 1H, Ar-H), 8.23–8.26 (m, 1H, Ar-H), 7.67–7.69 (d, 1H, Ar-H, *J* = 8 Hz), 7.59–7.61 (d, 2H, Ar-H, *J* = 8 Hz), 7.33–7.35 (d, 1H, Ar-H, *J* = 8 Hz), 7.10 (s, 1H, –CH=N), 4.24 (s, 3H, –OCH_3), 3.88 (s, 3H, –OCH_3). ***^{13}C NMR (100 MHz, DMSO-d_6, δ ppm):*** 166.39, 163.23, 158.63, 158.01, 157.55, 154.13, 143.68, 139.00, 132.87, 129.87, 129.79, 129.57, 125.01, 123.31, 120.60, 120.47, 117.14, 108.95, 40.07, 24.27. ***ESI-MS:*** *m/z* = 392.8 $[M]^+$.

(Z)-7-chloro-2-methoxy-10-(2-(2-methoxybenzylidene)hydrazineyl)benzo[b][1,5] naphthyridine (3f)

Brown crystalline solid; yield 92%; m.p. 230–232 °C; $C_{21}H_{17}ClN_4O_2$ (MW: 392.84 g/mol). ***IR (ATR, cm^{-1}):*** 3299 (N–H str., hydrazone), 2914 (C–H str., OCH_3), 1657 (C=N str., hydrazone), 1600 (C=C Ar str.), 1537, 1512 (C=C Ar str.), 1403, 1365 (C–N str.), 1287, 1237 (C–O–C str., OCH_3, ortho-substituted), 1030 (C–O str.), 858, 819 (Ar C–H o.o.p. bend.), 785, 742 (Ar C–H o.o.p. bend.). ***^{1}H NMR (400 MHz, DMSO-d_6, δ ppm):*** 9.96 (s, 1H, –NH), 9.64 (s, 1H, Ar-H), 8.72 (s, 1H, Ar-H), 8.16–8.18 (d, 1H, Ar-H, *J* = 8 Hz), 7.83 (s, 1H, Ar-H), 7.60–7.62 (d, 2H, Ar-H, *J* = 8 Hz), 7.49–7.51 (d, 1H, Ar-H, *J* = 8 Hz), 7.40 (s, 1H, Ar-H), 7.32–7.34 (d, 1H, Ar-H, *J* = 8 Hz), 6.94 (s, 1H, –CH=N), 4.20 (s, 3H, –OCH_3), 3.90 (s, 3H, –OCH_3). ***^{13}C NMR (100 MHz, DMSO-d_6, δ ppm):*** 163.23, 158.63, 155.73, 154.34, 154.13, 143.68, 139.00, 132.87, 129.79, 129.57, 125.01, 123.31, 121.51, 120.60, 117.14, 108.95, 40.07. ***ESI-MS:*** *m/z* = 393 $[M+H]^+$.

Molecular Docking Studies

Molecular docking studies of all synthesized compounds **3a–f** were performed against the EGFR kinase crystal structure (PDB ID: 3EQM, resolution: 2.40 Å) retrieved from the RCSB Protein Data Bank, using the Glide module (Standard Precision/Extra Precision mode) within the Schrödinger Maestro suite (Schrödinger LLC, New York, NY, USA). The protein was prepared using the Protein Preparation Wizard with protonation states assigned at physiological pH 7.0 using PROPKA, and energy minimization was performed with the OPLS4 force field until the heavy-atom RMSD converged to 0.30 Å from the original crystallographic coordinates. Ligand structures were prepared using the LigPrep module with ionization states generated at pH 7.0 ± 2.0 using Epik. The receptor grid was centered on the co-crystallized ligand within the ATP-binding pocket, with an inner box of 10 Å × 10 Å × 10 Å and an outer box of 30 Å × 30 Å × 30 Å. Validation of the docking protocol was confirmed by re-docking the co-crystallized reference ligand, which reproduced the experimental binding pose with an RMSD of 0.82 Å, well within the accepted threshold of 2.0 Å. The GlideScore (kcal/mol) was used as the primary ranking metric, and binding interactions were visualized using the Ligand Interaction Diagram tool in Maestro.

Conclusion:

In summary, six novel benzo[b][1,5]naphthyridine–arylhydrazone hybrid derivatives **(3a–f)** were successfully synthesized through a concise two-step route involving selective SNAr hydrazination and acid-catalyzed condensation, and fully characterized by IR, ^{1}H NMR, ^{13}C NMR, and ESI-MS. The integrated study comprising in vitro MTT-based antiproliferative evaluation, molecular docking against EGFR kinase (PDB: 3EQM), NMA-based molecular dynamics, and DFT calculations at the B3LYP/6-311G(d,p) level consistently identified compound **3a** as the lead molecule of the series.

Compound **3a,** bearing the strongly electron-donating 4-(dimethylamino)phenyl group, demonstrated the most potent MCF-7 antiproliferative activity (IC_{50} = 1.02 ± 0.36 μM), the highest EGFR docking affinity (–8.166 kcal/mol, exceeding ellipticine by 1.47 kcal/mol), and superior DFT electronic parameters including the smallest HOMO–LUMO gap (1.5922 eV), highest softness (S = 1.2561 eV^{-1}), and largest dipole moment (8.0136 D). NMA validated the stability of the 3a–EGFR complex through low binding-site deformability, satisfactory PDB–NMA B-factor correlation, low first eigenvalue, and cooperative N-lobe/C-lobe cross-correlated motions. The overall SAR trend **(3a > 3e > 3f > 3c > 3d > 3b)** confirmed that electron-donating substituents, especially strong para-donors, on the hydrazone aryl ring are the primary electronic drivers of antiproliferative potency. These results validate

pharmacophoric hybridization of the planar pyridoquinoline scaffold with hydrazone as an effective strategy for EGFR-targeted anticancer drug design, and compound **3a** is proposed as a promising lead candidate warranting further optimization, ADMET profiling, and in vivo evaluation.

Funding

We are also grateful for financial support from SHODH – Scheme of Developing High Quality Research, Knowledge Consortium of Gujarat, Education Department, Government of Gujarat. Letter Reference no:2023016937 in the form of research grants for this research work.

Data Availability

All data generated or analysed during this study are included in this published article and its supplementary information files.

References:

1. Sung, H., Ferlay, J., Siegel, R. L., Laversanne, M., Soerjomataram, I., Jemal, A., & Bray, F. (2021). Global cancer statistics 2020: GLOBOCAN estimates of incidence and mortality worldwide for 36 cancers in 185 countries. *CA: A Cancer Journal for Clinicians*, *71*(3), 209-249. https://doi.org/10.3322/caac.21660

2. Debela, D. T., Muzazu, S. G., Heraro, K. D., Ndalama, M. T., Mesele, B. W., Haile, D. C., Kitui, S. K., & Manyazewal, T. (2021). New approaches and procedures for cancer treatment: Current perspectives. *SAGE Open Medicine*, *9*, 20503121211034366. https://doi.org/10.1177/20503121211034366

3. Arora, A., & Scholar, E. M. (2005). Role of tyrosine kinase inhibitors in cancer therapy. *Journal of Pharmacology and Experimental Therapeutics*, *315*(3), 971–979. https://doi.org/10.1124/jpet.105.084145

4. Giaquinto, A. N., Sung, H., Newman, L. A., Freedman, R. A., Smith, R. A., Star, J., Jemal, A., & Siegel, R. L. (2024). Breast cancer statistics, 2024. *CA: A Cancer Journal for Clinicians*, *74*(6), 477–495. https://doi.org/10.3322/caac.21863

5. Kerru, N., Gummidi, L., Maddila, S., Gangu, K. K., & Jonnalagadda, S. B. (2020). A review of recent advances in nitrogen-containing molecules and their biological applications. *Molecules*, *25*(8), 1909. https://doi.org/10.3390/molecules25081909

6. Maheta, J. B., Lakhnotra, D. K., Shaikh, N. H., Dave, P. A., Pathak, D., Koradiya, S. B., & Bhola, Y. O. (2025). Synthesis, Spectroscopic Characterization, and DFT-Assisted Molecular Docking Analysis of Novel Thiazole–Coumarin–Sulfonamide Hybrids with Antimicrobial and Antioxidant Potential. *Journal of Molecular Structure*, 144824. https://doi.org/10.1016/j.molstruc.2025.144824

7. Afzal, O., Kumar, S., Haider, M. R., Ali, M. R., Kumar, R., Jaggi, M., & Bawa, S. (2015). A review on the anticancer potential of bioactive heterocyclic quinoline. *European Journal of Medicinal Chemistry*, *97*, 871-910. https://doi.org/10.1016/j.ejmech.2014.07.044

8. Solomon, V. R., & Lee, H. (2011). Quinoline as a privileged scaffold in cancer drug discovery. *Current Medicinal Chemistry*, *18*(10), 1488-1508. https://doi.org/10.2174/092986711795328382

9. Lakhnotra, D. K., Maheta, J. B., Shaikh, N. H., Ram I. M., and Bhola Y. O., Gandhi, S., Koradiya, S. B., Maheta, J. B., Shaikh, N. H., Bhola, Y. O., & Koradiya, S. B. (2025). Design, synthesis, and biological evaluation of schiff base derivatives incorporating quinoline-1,2,3-triazole moieties: Antimicrobial and anticancer activities, DFT simulations, and molecular docking studies. *Journal of Molecular Structure*, *1352*, 144452. https://doi.org/10.1016/j.molstruc.2025.144452

10. Faria, J. V., Vegi, P. F., Miguita, A. G., dos Santos, M. S., Boechat, N., & Bernardino, A. M. (2017). Recently reported biological activities of pyrazole derivatives. *Bioorganic & Medicinal Chemistry*, *25*(21), 5891-5903. https://doi.org/10.1016/j.bmc.2017.09.035

11. Grosch, S., Maier, T. J., Schiffmann, S., & Geisslinger, G. (2006). Cyclooxygenase-2 (COX-2)-independent anticarcinogenic effects of selective COX-2 inhibitors. *Journal of the National Cancer Institute*, *98*(11), 736-747. https://doi.org/10.1093/jnci/djj206

12. Viegas-Junior, C., Danuello, A., da Silva Bolzani, V., Barreiro, E. J., & Fraga, C. A. M. (2007). Molecular hybridization: A useful tool for designing new drug prototypes. *Current Medicinal Chemistry*, *14*(17), 1829-1852. https://doi.org/10.2174/092986707781058805

13. Decker, M. (2011). Hybrid molecules incorporating natural products: Applications in cancer therapy and neurodegenerative disorders *Current Medicinal Chemistry*, *18*(11), 1464-1475. https://doi.org/10.2174/092986711795328355.

14. Shaikh, N. H., Maheta, J. B., Lakhnotra, D. K., Ram, I. M., Bhola, Y. O., & Jain, S. A. (2025). Computational and Experimental Insights into the Anticancer and Antimicrobial Activity of Coumarin-1,2,3-Triazole Derivatives: A Study Based on DFT, Docking, ADME, and In Vitro Assays. *ChemistrySelect*, *10*(36). https://doi.org/10.1002/slct.202503975

15. Cioc, R. C., Ruijter, E., & Orru, R. V. (2014). Multicomponent reactions: Advanced tools for sustainable organic synthesis. *Green Chemistry*, *16*(6), 2958-2975. https://doi.org/10.1039/C4GC00013G

16. Maheta, J. B., Shaikh, N. H., Lakhnotra, D. K., Ram, I. M., Thakkar, A. B., Thakor, P., Subramanian, R., & Bhola, Y. O. (2025). "Triazole-oxadiazole-based schiff bases as potential kinase inhibitors: synthesis, DFT studies, molecular docking and anticancer evaluation." *Results in Chemistry*, *18*, 102727. https://doi.org/10.1016/j.rechem.2025.102727

17. Rotstein, B. H., Zaretsky, S., Rai, V., & Yudin, A. K. (2014). Small heterocycles in multicomponent reactions. *Chemical Reviews*, *114*(16), 8323-8359. https://doi.org/10.1021/cr400615v

18. Bray, F., Ferlay, J., Soerjomataram, I., Siegel, R. L., Torre, L. A., & Jemal, A. (2018). Global cancer statistics 2018: GLOBOCAN estimates of incidence and mortality worldwide for 36 cancers in 185 countries. *CA: A Cancer Journal for Clinicians*, *68*(6), 394-424. https://doi.org/10.3322/caac.21492

19. De Vera, C., Crespín, G. D., Daranas, A. H., Looga, S. M., Lillsunde, K., Tammela, P., Perälä, M., Hongisto, V., Virtanen, J., Rischer, H., Muller, C., Norte, M., Fernández, J., & Souto, M. (2018). Marine microalgae: a promising source of new bioactive compounds. *Marine Drugs*, *16*(9), 317. https://doi.org/10.3390/md16090317

Supplementary Files

This is a list of supplementary files associated with this preprint. Click to download.

- supplemenetrydata.docx